AUT Journal of Mechanical Engineering

AUT J. Mech. Eng., 2(2) (2018) 127-136
DOI: 10.22060/ajme.2018.13862.5693

A Simplified Description of the Uniaxial Tensile Test Used for Calibrating Constitutive Models of Orthotropic Porous Sheet Metals

A. Kami[1*], D.-S. Comsa[2]

[1] Mechanical Engineering Department, Semnan University, Semnan, Iran
[2] CERTETA Research Centre, Technical University of Cluj-Napoca, Cluj-Napoca, Romania

ABSTRACT: In the present work, a simplified model of the uniaxial tensile test is developed for orthotropic metallic sheets. This model is mainly established for tensile test analysis and calibration of material parameters. The constitutive equations included in the model are based on an anisotropic Gurson-Tvergaard-Needleman model combined with the Hill 1948 quadratic yield criterion. At first, a detailed description of the constitutive equations along with their computer implementation is presented. Then, by comparing the force and void evolution diagrams predicted by the model with numerical and experimental results the efficiency and accuracy of the model are assessed. Finally, the effect of different parameters on the traction force and evolution of voids during uniaxial tensile tests are studied. The material parameters used in the calibration procedure are as follows: initial void volume fraction, two adjusting parameters, nucleation of void volume fraction, standard deviation, mean value of void nucleation strain, and sample orientation with respect to the rolling direction. The tests performed by the authors prove the capability of the simplified model to describe accurately the mechanical response of orthotropic sheet metals.

Review History:

Received: 23 December 2017
Revised: 29 May 2018
Accepted: 30 May 2018
Available Online: 20 June 2018

Keywords:

Gurson damage model
Gurson-Tvergaard-Needleman
Tensile test
Parameter calibration
Anisotropy

1- Introduction

During straining of ductile metals voids grow and coalesce, which result in softening and damage. The early observations of this phenomenon go back to Tipper [1] and Puttick [2]. McClintock [3] and Rice and Tracey [4] are the first researchers who formulated a model to describe the damage of ductile metals caused by voids growth. However, the well-known model in this subject is the one developed by Gurson [5]. He used an upper-bound approach to model the growth of a spherical void inside a characteristic volume element. Later, Gurson's model [5] has been enhanced by Tvergaard and Needleman [6, 7] in a formulation known as Gurson-Tvergaard-Needleman (GTN) model. The use of the GTN model has been further extended by its modification to account for shear dominated loads [8] or plastic anisotropy [9, 10].

One important aspect in the application of GTN models is the calibration of its parameters. Different approaches have been proposed for this purpose, a few of them being mentioned here. Abendroth and Kuna [11] trained an artificial neural network for predicting the load vs. displacement curve of the small punch test. They were able to identify the GTN model parameters by minimizing the error between the experimental load vs. displacement curve and the one predicted by the neural network function. Broggiato et al. [12] estimated the GTN parameters using experimental data collected from digital image processing of a notched specimen during tensile test. Kami et al. [13] measured the values of the major and minor limit strains at the surface of hydraulic bulge test specimens at the onset of necking. They calculated the GTN model parameters by minimizing the error between the experimental limit strains and the limit strains obtained from numerical simulations of a hydraulic bulge test. In another approach, a genetic algorithm optimization tool was employed to find the GTN parameters such that the error between numerical predictions and experimental measurements of the force–displacement data for smooth round bar and dog-bone specimens is minimized [14]. Of course, a long list of literature related to the calibration of the GTN model parameters could be presented. But they are omitted for brevity.

The literature survey shows that the load-displacement data obtained from the uniaxial tensile tests are widely used for calibrating the GTN model parameters (see [14-16] for example). In order to facilitate the application of GTN models, especially for calibration purposes, a simplified model of the uniaxial tensile test has been developed by the authors. This model is able to predict the force-displacement curve obtained in a uniaxial tensile test. The simplified model could be programmed as a separate code and it is not required to be implemented in any finite element program. Furthermore, almost all researchers focused on the identification of a reduced set of the GTN model parameters. However, the simplified model could be used for calibrating a full set of parameters affecting the material behavior up to the ultimate strength point on the uniaxial stress-strain curve (i.e., all GTN parameters except the critical void volume fraction, f_C, and final void volume fraction, f_F). The model developed in the present paper is based on the work of Kami et al. [9].

The GTN constitutive equations based on Hill [17] anisotropic yield criterion are presented in the next section. Then, the

Corresponding author, E–mail: akami@semnan.ac.ir

simplified model of the tensile test is formulated. Finally, the model is used to show the effect of the initial void volume fraction, f_0, adjusting parameters, q_1 and q_2, nucleation void volume fraction, f_N, standard deviation, S_N, mean value of void nucleation strain, $\bar{e}_N^{(p)}$, and sample orientation with respect to the rolling direction on the evolution of force and voids during loading.

2- Formulation of the Constitutive Model

In this section, the GTN constitutive equations based on Hill [17] anisotropic yield criterion are described for the case of a ductile porous sheet metal exhibiting plastic orthotropy. One assumes that the sheet metal is initially flat, its orthotropy frame being defined by the Rolling Direction (RD) (axis 1), Transverse Direction (TD) (axis 2) and Normal Direction (ND) (axis 3). The following symbols will denote macroscopic strain and stress quantities:

– components of the logarithmic strain tensor separable into elastic $\varepsilon_{ij}^{(e)} = \varepsilon_{ji}^{(e)}$ and plastic $\varepsilon_{ij}^{(p)} = \varepsilon_{ji}^{(p)}$ parts, i.e.,

$$\varepsilon_{ij} = \varepsilon_{ij}^{(e)} + \varepsilon_{ij}^{(p)} \tag{1}$$

– components of the Cauchy stress tensor $\sigma_{ij} = \sigma_{ji}$

– hydrostatic pressure

$$p = -\sigma_{ii} / 3. \tag{2}$$

– Hill 1948 equivalent stress [17]

$$\bar{\sigma} = \sqrt{\sigma_{ij} P_{ijk\ell} \sigma_{k\ell}}, \tag{3}$$

where P_{ijkl} are components of a fourth-order tensor by means of which the constitutive model approximates the plastic orthotropy of the sheet metal. These material parameters are subjected to the constraints

$$P_{ijk\ell} = P_{jik\ell} = P_{ij\ell k} = P_{k\ell ij}, \qquad P_{iik\ell} = 0. \tag{4}$$

In the case of orthotropic metallic sheets, Eq. (3) usually gets the explicit form:

$$\bar{\sigma} = \{ \frac{1}{(r_0+1) r_{90}} [r_0 (\sigma_{22}-\sigma_{33})^2 + r_{90} (\sigma_{33}-\sigma_{11})^2 + r_0 r_{90} (\sigma_{11}-\sigma_{22})^2 + 3(r_0+1) r_{90} (\sigma_{23}\sigma_{32} + \sigma_{31}\sigma_{13}) + (r_0+r_{90})(2r_{45}+1)\sigma_{12}\sigma_{21}]\}^{1/2}, \tag{5}$$

where r_0 , r_{45} and r_{90} are experimental values of the Lankford coefficient corresponding to the planar directions respectively defined by the angles θ=0°, 45° and 90° with reference to RD. It is not difficult to prove that Eq. (3) reduces to Eq. (5) if (see also conditions (4))

$$\begin{aligned}
&P_{ijkl} = 0, \text{ except for} \\
&P_{1111} = 1, \\
&P_{2222} = r_0 (r_{90}+1) / [(r_0+1) r_{90}], \\
&P_{3333} = (r_0+r_{90}) / [(r_0+1) r_{90}], \\
&P_{1122} = P_{2211} = -r_0 / (r_0+1), \\
&P_{2233} = P_{3322} = -r_0 [(r_0+1) r_{90}], \\
&P_{3311} = P_{1133} = -1 / (r_0+1), \\
&P_{1212} = P_{1221} = P_{2112} = P_{2121} = (r_0+r_{90})(2r_{45}+1) / [4(r_0+1) r_{90}], \\
&P_{2323} = P_{2332} = P_{3223} = P_{3232} = P_{3131} = P_{3113} = P_{1331} = P_{1313} = 3/4.
\end{aligned} \tag{6}$$

Two other strain/stress parameters will be associated to the fully dense matrix material: $\bar{e}^{(p)}$ – equivalent plastic strain ($\bar{e}^{(p)} \geq 0$, $\dot{\bar{e}}^{(p)} \geq 0$) and Y – yield stress defined as a strictly positive function of $\bar{e}^{(p)}$ by means of the hardening law $Y = Y[\bar{e}^{(p)}] > 0$.

The elasticity of the sheet metal is described by the isotropic Hooke's law

$$\sigma_{ij} = \frac{E}{1+\nu} \left[\varepsilon_{ij}^{(e)} + \frac{\nu}{1-2\nu} \varepsilon_{\ell\ell}^{(e)} \delta_{ij} \right]. \tag{7}$$

In this relationship, E and ν denote Young's modulus and Poisson's ratio, respectively.

The plastic part of the constitutive model is based on the GTN potential [6, 7]

$$\Phi = \left(\frac{\bar{\sigma}}{Y} \right)^2 + q_1 f^* \left[2\cosh\left(-q_2 \frac{3p}{2Y} \right) - q_1 f^* \right] - 1, \tag{8}$$

where

$$f^* = \begin{cases} f, & \text{if} \quad f \leq f_C, \\ f_C + \dfrac{f_F^* - f_C}{f_F - f_C} (f - f_C), & \text{if} \quad f_C < f < f_F, \quad \text{with } f_F^* = \dfrac{1}{q_1} \\ f_F^*, & \text{if} \quad f \geq f_F, \end{cases} \tag{9}$$

is a porosity parameter depending on the void volume fraction f. The quantities denoted as q_1, q_2, f_C, and f_F in Eqs. (8) and (9) are material constants. The condition $\Phi \leq 0$ defines all the admissible stress states. More precisely, $\Phi < 0$ in elastic states and $\Phi = 0$ in the elastoplastic states.

The flow rule associated to the potential Φ can be expressed in the form

$$\dot{\varepsilon}_{ij}^{(p)} = \dot{\lambda} \frac{\partial \Phi}{\partial \sigma_{ij}}, \qquad \text{with} \begin{cases} \dot{\lambda} = 0, & \text{if } \Phi < 0, \\ \dot{\lambda} \geq 0, & \text{if } \Phi = 0, \end{cases} \tag{10}$$

or, if Eqs. (8), (3) and (4) are taken into account,

$$\dot{\varepsilon}_{ij}^{(p)} = \frac{1}{\bar{\sigma}} \dot{\bar{\varepsilon}}^{(p,dev)} P_{ijk\ell} \sigma_{k\ell} + \frac{1}{3} \dot{\bar{\varepsilon}}^{(p,vol)} \delta_{ij}, \tag{11}$$

where

$$\dot{\bar{\varepsilon}}^{(p,dev)} = \dot{\lambda} \frac{\partial \Phi}{\partial \bar{\sigma}}, \qquad \dot{\bar{\varepsilon}}^{(p,vol)} = -\dot{\lambda} \frac{\partial \Phi}{\partial p}, \tag{12}$$

and

$$\frac{\partial \Phi}{\partial \overline{\sigma}} = \frac{2\overline{\sigma}}{Y^2}, \qquad \frac{\partial \Phi}{\partial p} = -3q_1 q_2 \frac{f^*}{Y} \sinh\left(-q_2 \frac{3p}{2Y}\right). \quad (13)$$

Eq. (12) allow deducing the following consistency condition that accompanies the constraint Φ = 0 in the elastoplastic states of the sheet metal [9]:

$$\dot{\varepsilon}^{(p,dev)} \frac{\partial \Phi}{\partial p} + \dot{\varepsilon}^{(p,vol)} \frac{\partial \Phi}{\partial \overline{\sigma}} = 0. \quad (14)$$

The evolution of the parameter $\bar{e}^{(p)}$ is controlled by the equivalent plastic work rule

$$\sigma_{ij} \dot{\varepsilon}_{ij}^{(p)} = (1-f) Y \dot{\overline{e}}^{(p)}. \quad (15)$$

With the help of Eqs. (11) and (2) to (4), Eq. (15) becomes

$$\overline{\sigma} \dot{\overline{\varepsilon}}^{(p,dev)} - p \dot{\overline{\varepsilon}}^{(p,vol)} = (1-f) Y \dot{\overline{e}}^{(p)}. \quad (16)$$

As for the parameter f, its time derivative cumulates the growth of the existing voids $\dot{f}^{(g)}$ and the nucleation of new voids $\dot{f}^{(n)}$:

$$\dot{f} = \dot{f}^{(g)} + \dot{f}^{(n)}. \quad (17)$$

$\dot{f}^{(g)}$ is directly related to the volumetric part of the plastic strain rate tensor (see also Eqs. (11) and (4)),

$$\dot{f}^{(g)} = (1-f) \dot{\overline{\varepsilon}}^{(p,vol)}, \quad (18)$$

while $\dot{f}^{(n)}$ is a function of the equivalent plastic strain and its time derivative:

$$\dot{f}^{(n)} = A[\overline{e}^{(p)}] \dot{\overline{e}}^{(p)}. \quad (19)$$

The multiplier $A[\bar{e}^{(p)}]$ on the right-hand side of Eq. (19) has the expression

$$A[\overline{e}^{(p)}] = \begin{cases} \dfrac{f_N}{s_N \sqrt{2\pi}} \exp\left\{-\dfrac{1}{2}\left[\dfrac{\overline{e}^{(p)} - \overline{e}_N^{(p)}}{s_N}\right]^2\right\}, & \text{if } p < 0, \\ 0, & \text{if } p \geq 0, \end{cases} \quad (20)$$

where f_N, s_N and $\bar{e}^{(p)}$ are material constants. One may notice that, according to Eqs. (19) and (20), $\dot{f}^{(n)}$ is different from zero only in the hydrostatic traction states individualized by the condition $p < 0$ (see Eq. (2)). The numerical implementation of the abovementioned constitutive equations (GTN model based on Hill's quadratic yield stress) as a VUMAT routine is described in Kami et al. [9].

3- Simplified Model of the Uniaxial Tensile Test

This section presents an efficient methodology that can be used to calculate force vs. elongation diagrams for tensile specimens separated along RD from metallic sheets exhibiting plastic orthotropy. The procedure has been developed with the aim of speeding up the identification of the porous elastoplastic constitutive model. Its efficiency is ensured by the following hypotheses that simplify the simulation of a uniaxial tensile test:

- The specimen gauge is a region characterized by uniformly distributed state parameters. In this material volume, the plastic orthotropy frame remains coincident with RD (axis 1), TD (axis 2) and ND (axis 3).
- The traction load induces a uniaxial stress state in the gauge:

$$\sigma_{ij} = 0, \text{ if } i \neq 1 \text{ or } j \neq 1,$$
$$\varepsilon_{ij}^{(e)} = 0 \text{ and } \varepsilon_{ij}^{(p)} = 0, \text{ if } i \neq j. \quad (21)$$

- The gauge is initially configured as a rectangular parallelepiped and preserves this characteristic shape during the tensile test (Fig. 1).

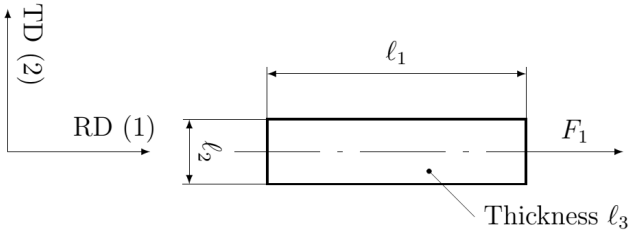

Fig. 1. Gauge region of a tensile specimen separated from a metallic sheet along RD and loaded by an axial force F_1.

Of course, a model based on such assumptions cannot describe the necking and post-necking response of the specimen. Due to this fact, its applicability is limited to the tensile states characterized by void volume fractions taking values in the range

$$0 \leq f \leq f_C, \quad (22)$$

for which Eq. (9) reduces to the form

$$f^* = f. \quad (23)$$

The gauge elongation and the corresponding axial force are easily expressible as functions of the non-zero strain and stress components:

$$\ell_1 - {}^0\ell_1 = {}^0\ell_1 \left[\exp(\varepsilon_{11}) - 1\right],$$
$$F_1 = \sigma_{11} \ell_2 \ell_3 = \sigma_{11} {}^0\ell_2 {}^0\ell_3 \exp(\varepsilon_{22} + \varepsilon_{33}). \quad (24)$$

The following notations have been introduced in these relationships (see Fig. 1): ${}^0l_1$, ${}^0l_2$, ${}^0l_3$ are initial dimensions of the gauge, l_1, l_2, l_3 are current dimensions of the gauge, and F_1 is the current value of the axial force. Eq. (24) can be exploited to calculate a point of the diagram force F_1 vs. elongation l_1 - ${}^0l_1$ whenever the state parameters σ_{11}, ε_{11} and $\varepsilon_{22}+\varepsilon_{33}$ are available. The discussion below will focus on the evaluation of σ_{11}, ε_{11} and $\varepsilon_{22}+\varepsilon_{33}$ using the porous elastoplastic constitutive model particularized for the uniaxial tensile test:

- Additive decomposition of the longitudinal, transverse and through-thickness logarithmic strains (see Eqs. (1) and (21)):

$$\varepsilon_{ii} = \varepsilon_{ii}^{(e)} + \varepsilon_{ii}^{(p)} \quad \text{(no sum)} \quad (25)$$

- Isotropic Hooke's law corresponding to the uniaxial stress state defined by Eq. (21):

$$\sigma_{11} = E\,\varepsilon_{11}^{(e)} = -E\,\varepsilon_{22}^{(e)} / \nu = -E\,\varepsilon_{33}^{(e)} / \nu \tag{26}$$

- GTN potential resulted from Eqs. (8), (2), (3), and (6), when conditions (21) and (23) are taken into account:

$$\Phi = \left(\frac{\sigma_{11}}{Y}\right)^2 + q_1 f\left(2\cosh\frac{q_2\sigma_{11}}{2Y} - q_1 f\right) - 1 \tag{27}$$

- Flow rule defined by Eqs. (11), (3) and (6) together with Eq. (21):

$$\begin{aligned}
\dot{\varepsilon}_{11}^{(p)} &= \dot{\bar{\varepsilon}}^{(p,dev)} + \frac{1}{3}\dot{\bar{\varepsilon}}^{(p,vol)},\\
\dot{\varepsilon}_{22}^{(p)} &= -\frac{r_0}{r_0+1}\dot{\bar{\varepsilon}}^{(p,dev)} + \frac{1}{3}\dot{\bar{\varepsilon}}^{(p,vol)},\\
\dot{\varepsilon}_{33}^{(p)} &= -\frac{1}{r_0+1}\dot{\bar{\varepsilon}}^{(p,dev)} + \frac{1}{3}\dot{\bar{\varepsilon}}^{(p,vol)}
\end{aligned} \tag{28}$$

- Consistency condition that accompanies the constraint $\Phi=0$ in any elastoplastic state (deduced from Eqs. (14), (13), (2), (3), (6), (21), and (23)):

$$\frac{\sigma_{11}}{Y}\dot{\bar{\varepsilon}}^{(p,vol)} - \frac{3}{2}q_1 q_2 f\,\sinh\left(\frac{q_2\sigma_{11}}{2Y}\right)\dot{\bar{\varepsilon}}^{(p,dev)} = 0 \tag{29}$$

- Equivalent plastic work rule given by Eqs. (16), (2), (3), (6), and (21):

$$\frac{\sigma_{11}}{Y}\left[\dot{\bar{\varepsilon}}^{(p,dev)} + \frac{1}{3}\dot{\bar{\varepsilon}}^{(p,vol)}\right] = (1-f)\,\dot{\bar{e}}^{(p)} \tag{30}$$

- Law that controls the change of the void volume fraction (obtained from Eqs. (17) to (20), (2), and (21), bearing in mind that $p=-\sigma_{11}/3 < 0$ is a property of all inelastic states):

$$\dot{f} = (1-f)\,\dot{\bar{\varepsilon}}^{(p,vol)} + \frac{f_N}{s_N\sqrt{2\pi}}\exp\left\{-\frac{1}{2}\left[\frac{\bar{e}^{(p)} - \bar{e}_N^{(p)}}{s_N}\right]^2\right\}\dot{\bar{e}}^{(p)}. \tag{31}$$

The simulation of the uniaxial tensile test consists in a sequence of small time increments $t \to t+\Delta t$. The configuration of the gauge corresponding to the moment t is a reference state, its parameters ${}^t\sigma_{11}$, ${}^t\varepsilon_{11}$, ${}^t\varepsilon_{22}$, ${}^t\varepsilon_{33}$, ${}^t\bar{e}^{(p)}$ and ${}^t f$ being known quantities. Together with this data, the increment of the longitudinal logarithmic strain:

$${}_t^{t+\Delta t}\varepsilon_{11} = \int_t^{t+\Delta t}\dot{\varepsilon}_{11}\,\mathrm{d}\tau \tag{32}$$

is also given as input. The objective of each simulation step consists in evaluating the current state parameters ${}^{t+\Delta t}\sigma_{11}$, ${}^{t+\Delta t}\varepsilon_{11}$, ${}^{t+\Delta t}\varepsilon_{22}$, ${}^{t+\Delta t}\varepsilon_{33}$, ${}^{t+\Delta t}\bar{e}^{(p)}$ and ${}^{t+\Delta t}f$. The value of ${}^{t+\Delta t}\sigma_{11}$ can be determined using incremental forms of Eqs. (26) and (25) in combination with Eqs. (32) and (28):

$${}^{t+\Delta t}\sigma_{11} = {}^{t+\Delta t}\sigma_{11}^{(e)} - E\left[{}_t^{t+\Delta t}\bar{\varepsilon}^{(p,dev)} + \frac{1}{3}{}_t^{t+\Delta t}\bar{\varepsilon}^{(p,vol)}\right], \tag{33}$$

where

$${}^{t+\Delta t}\sigma_{11}^{(e)} = {}^{t}\sigma_{11} + E\,{}_t^{t+\Delta t}\varepsilon_{11}, \tag{34}$$

$$\begin{aligned}
{}_t^{t+\Delta t}\bar{\varepsilon}^{(p,dev)} &= {}^{t+\Delta t}\dot{\bar{\varepsilon}}^{(p,dev)}\Delta t,\\
{}_t^{t+\Delta t}\bar{\varepsilon}^{(p,vol)} &= {}^{t+\Delta t}\dot{\bar{\varepsilon}}^{(p,vol)}\Delta t.
\end{aligned} \tag{35}$$

Eq. (34) defines a stress level that would occur in the current configuration of the gauge if the incremental logarithmic strain ${}_t^{t+\Delta t}\varepsilon_{11}$ were purely elastic. In practice, ${}^{t+\Delta t}\sigma_{11}{}^{(e)}$ is the first quantity that must be evaluated. When ${}^{t+\Delta t}\sigma_{11}{}^{(e)}$ is available, Eq. (27) allows calculating the trial GTN function:

$${}^{t+\Delta t}\Phi^{(e)} = \left\{\frac{{}^{t+\Delta t}\sigma_{11}^{(e)}}{Y\left[{}^t\bar{e}^{(p)}\right]}\right\}^2 + q_1{}^t f\left\{2\cosh\frac{q_2\,{}^{t+\Delta t}\sigma_{11}^{(e)}}{2Y\left[{}^t\bar{e}^{(p)}\right]} - q_1{}^t f\right\} - 1. \tag{36}$$

If ${}^{t+\Delta t}\Phi^{(e)} \le 0$, the hypothesis of an elastic strain increment is correct. In such a situation, the current state parameters are immediately evaluable using already known quantities (see also Eqs. (26) and (32)):

$$\left.\begin{aligned}
{}^{t+\Delta t}\sigma_{11} &= {}^{t+\Delta t}\sigma_{11}^{(e)},\\
{}^{t+\Delta t}\varepsilon_{11} &= {}^{t}\varepsilon_{11} + {}_t^{t+\Delta t}\varepsilon_{11},\\
{}^{t+\Delta t}\varepsilon_{22} + {}^{t+\Delta t}\varepsilon_{33} &= {}^{t}\varepsilon_{22} + {}^{t}\varepsilon_{33} - 2\nu\,{}_t^{t+\Delta t}\varepsilon_{11},\\
{}^{t+\Delta t}\bar{e}^{(p)} &= {}^{t}\bar{e}^{(p)},\\
{}^{t+\Delta t}f &= {}^{t}f,
\end{aligned}\right\} \text{ if } {}^{t+\Delta t}\Phi^{(e)} \le 0. \tag{37}$$

If ${}^{t+\Delta t}\Phi^{(e)} > 0$, the gauge evolves through elastoplastic states, the increments ${}_t^{t+\Delta t}\bar{\varepsilon}^{(p,dev)}$ and ${}_t^{t+\Delta t}\bar{\varepsilon}^{(p,vol)}$ on the right-hand side of Eq. (33) being two extra unknowns. In this case, it is convenient to manipulate Eq. (33) under the normalized form

$${}^{t+\Delta t}\hat{\sigma}_{11} = {}^{t+\Delta t}\hat{\sigma}_{11}^{(e)} - \frac{E}{Y\left[{}^{t+\Delta t}\bar{e}^{(p)}\right]}\left[{}_t^{t+\Delta t}\bar{\varepsilon}^{(p,dev)} + \frac{1}{3}{}_t^{t+\Delta t}\bar{\varepsilon}^{(p,vol)}\right], \tag{38}$$

where

$${}^{t+\Delta t}\hat{\sigma}_{11} = {}^{t+\Delta t}\sigma_{11}/Y\left[{}^{t+\Delta t}\bar{e}^{(p)}\right], \tag{39}$$

$${}^{t+\Delta t}\hat{\sigma}_{11}^{(e)} = {}^{t+\Delta t}\sigma_{11}^{(e)}/Y\left[{}^{t+\Delta t}\bar{e}^{(p)}\right], \tag{40}$$

Due to the inelastic character of the current state, Eq. (38) must be accompanied by the following constraints:

- First consistency condition ${}^{t+\Delta t}\Phi = 0$, i.e., (see Eqs. (27) and (39))

$$ {}^{t+\Delta t}\hat{\sigma}_{11}^{2} + q_1\,{}^{t+\Delta t}f\left[2\cosh\left(\frac{q_2}{2}\,{}^{t+\Delta t}\hat{\sigma}_{11}\right) - q_1\,{}^{t+\Delta t}f\right] = 1 \qquad (41) $$

- Incremental form of the second consistency condition defined by Eq. (29) together with Eqs. (35) and (39):

$$ {}^{t+\Delta t}\hat{\sigma}_{11}\,{}^{t+\Delta t}_{t}\overline{\varepsilon}^{(p,vol)} - \frac{3}{2}q_1q_2\,{}^{t+\Delta t}f\,\sinh\left(\frac{q_2}{2}\,{}^{t+\Delta t}\hat{\sigma}_{11}\right)\,{}^{t+\Delta t}_{t}\overline{\varepsilon}^{(p,dev)} = 0 \qquad (42) $$

- Incremental form of the equivalent plastic work rule defined by Eq. (30), the backward Euler approximation:

$$ {}^{t+\Delta t}\overline{e}^{(p)} - {}^{t}\overline{e}^{(p)} = {}^{t+\Delta t}\dot{\overline{e}}^{(p)}\Delta t, \qquad (43) $$

in combination with Eqs. (35) and (39):

$$ {}^{t+\Delta t}\hat{\sigma}_{11}\left[{}^{t+\Delta t}_{t}\overline{\varepsilon}^{(p,dev)} + \frac{1}{3}\,{}^{t+\Delta t}_{t}\overline{\varepsilon}^{(p,vol)}\right] = \left(1-{}^{t+\Delta t}f\right)\left[{}^{t+\Delta t}\overline{e}^{(p)} - {}^{t}\overline{e}^{(p)}\right] \qquad (44) $$

- Incremental form of the law that controls the change of the void volume fraction obtained from Eqs. (31), (35) and (43):

$$ {}^{t+\Delta t}f = {}^{t}f + \left(1-{}^{t+\Delta t}f\right)\,{}^{t+\Delta t}_{t}\overline{\varepsilon}^{(p,vol)} + \frac{f_N}{s_N\sqrt{2\pi}}\exp\left\{-\frac{1}{2}\left[\frac{{}^{t+\Delta t}\overline{e}^{(p)} - \overline{e}_N^{(p)}}{s_N}\right]^2\right\}\left[{}^{t+\Delta t}\overline{e}^{(p)} - {}^{t}\overline{e}^{(p)}\right]. \qquad (45) $$

It is not difficult to notice that Eqs. (44) and (45) allow expressing ${}^{t+\Delta t}_{t}\bar{\varepsilon}^{(p,dev)}$ and ${}^{t+\Delta t}_{t}\bar{\varepsilon}^{(p,vol)}$ as functions of the current state parameters ${}^{t+\Delta t}\hat{\sigma}_{11}$, ${}^{t+\Delta t}\bar{e}^{(p)}$ and ${}^{t+\Delta t}f$:

$$ {}^{t+\Delta t}_{t}\overline{\varepsilon}^{(p,dev)} = \frac{1}{{}^{t+\Delta t}\hat{\sigma}_{11}}\left(1-{}^{t+\Delta t}f\right)\left[{}^{t+\Delta t}\overline{e}^{(p)} - {}^{t}\overline{e}^{(p)}\right] - \frac{1}{3}\,{}^{t+\Delta t}_{t}\overline{\varepsilon}^{(p,vol)}, \qquad (46) $$

$$ {}^{t+\Delta t}_{t}\overline{\varepsilon}^{(p,vol)} = \frac{1}{1-{}^{t+\Delta t}f}\left\{{}^{t+\Delta t}f - {}^{t}f - \frac{f_N}{s_N\sqrt{2\pi}}\exp\left\{-\frac{1}{2}\left[\frac{{}^{t+\Delta t}\overline{e}^{(p)} - \overline{e}_N^{(p)}}{s_N}\right]^2\right\}\left[{}^{t+\Delta t}\overline{e}^{(p)} - {}^{t}\overline{e}^{(p)}\right]\right\} \qquad (47) $$

Eqs. (46) and (47) transform Eqs. (38), (41) and (42) into a nonlinear set having ${}^{t+\Delta t}\hat{\sigma}_{11}$, ${}^{t+\Delta t}\bar{e}^{(p)}$ and ${}^{t+\Delta t}f$ as unknowns. This set can be solved in a manner that closely follows the principles of the numerical scheme described by Kami et al. [9]. As soon as the solution is available, the current stress can be calculated using the relationship:

$$ {}^{t+\Delta t}\sigma_{11} = {}^{t+\Delta t}\hat{\sigma}_{11}Y\left[{}^{t+\Delta t}\overline{e}^{(p)}\right]. \qquad (48) $$

In the same time, Eqs. (32), (25), (26), (28), and (35) provide the following formulae that can be used together with Eqs. (46) and (47) for updating the longitudinal and cross-sectional strains of the gauge:

$$ {}^{t+\Delta t}\varepsilon_{11} = {}^{t}\varepsilon_{11} + {}^{t+\Delta t}_{t}\varepsilon_{11}, $$

$$ {}^{t+\Delta t}\varepsilon_{22} + {}^{t+\Delta t}\varepsilon_{33} = {}^{t}\varepsilon_{22} + {}^{t}\varepsilon_{33} - 2\nu\,{}^{t+\Delta t}_{t}\varepsilon_{11} - (1-2\nu)\,{}^{t+\Delta t}_{t}\overline{\varepsilon}^{(p,dev)} + \frac{2}{3}(1+\nu)\,{}^{t+\Delta t}_{t}\overline{\varepsilon}^{(p,vol)}. \qquad (49) $$

4- Results and Discussions

The simplified model of the tensile test allows calculating the force-displacement curve and the void evolution in an efficient manner. In what follows, the results of the model will be validated by comparison with experimental and numerical results. The effect of different parameters on the force and void evolution will be then studied.

4- 1- Validation of the proposed tensile test model

The experimental and numerical results presented by Kami et al. [16] have been used to validate the simplified model of the tensile test. Kami et al. [16] conducted tensile test experiments on AA6016-T4 aluminum alloy. With the help of these experiments, they defined the hardening law of AA6016-T4 alloy as $Y=525.77(\bar{e}^{(p)} + 0.01125)^{0.27}$. Other mechanical parameters of the AA6016-T4 alloy are listed in Table 1. Furthermore, the identified values of GTN model parameters based on the approach adopted by Kami et al. [16] are presented in Table 2. Kami et al. [16] determined the GTN model parameters by means of an identification procedure that combines the Response Surface Methodology (RSM) and the simulation of a uniaxial tensile test. The identification was accomplished by finding of values of the GTN parameters which resulted in the lowest error in the prediction of the experimental force-displacement curve. The values of f_0, f_N, f_C and f_F were calculated using this identification procedure. While, the values of the other parameters mentioned in Table 2 were chosen from literature.

Table 1. Mechanical properties of AA6016-T4 sheet [16]

Young's Modulus, [GPa]	Poisons's ratio, ν	Lankford coefficient		
		r_0	r_{45}	r_{90}
70	152	0.5529	0.4091	0.5497

By using the above-mentioned properties of AA6016-T4 sheet in the simplified model of the tensile test, the force-displacement curve of the tensile specimen was calculated. To determine the values of forces and elongations, the following dimensions of the gauge region were used: 80 mm length, 20 mm width, and 1 mm thickness. In Fig. 2, the force versus displacement (Δl) curve calculated by means of the simplified model is compared with the experimental and numerical curves presented by Kami et al. [16]. As shown in Fig. 2,

Table 2. GTN model parameters of AA6016-T4 sheet [16]

f_0	q_1	q_2	q_3	f_N	S_N	$\bar{e}_N^{(p)}$	f_C	f_F
0.00024	1.5	1.0	2.25	0.04155	0.1	0.3	0.04767	0.2

the predictions of the simplified model are almost coincident with the experimental and numerical results of Kami et al. [16]. It should be noted that the comparison is valid until reaching the Ultimate Tensile Force (UTF). The value of UTF determined by the simplified model (5571.56 N) is almost equal to the numerical UTF (5571.70 N). There is also a small difference (0.58% error) between the UTF value predicted by the simplified model and the experimental UTF (5604.24 N). The Ultimate Tensile Deformation (UTD) predicted by the simplified model is 19.44 mm (almost equal to the numerical UTD – 19.50 mm), which is 9.44% far from the experimental UTD – 17.76 mm. Although this difference might be acceptable, the authors believe that it could be reduced by modifying the adopted GTN model parameters, which in turn requires modifications in the identification procedure utilized by Kami et al. [16].

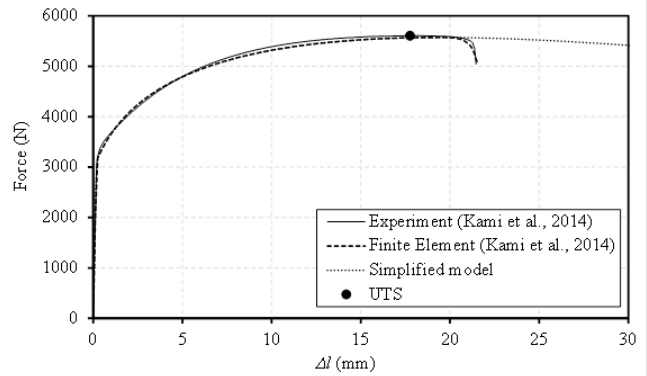

Fig. 2. Comparison of uniaxial traction forces predicted by the simplified model with the results of experiments and the finite element simulation presented in [16].

The voids evolution curves calculated by finite element simulation and the simplified model are compared in Fig. 3. From this figure one may notice that until the ultimate point (UTS) – 17.76 mm deformation – the voids evolution curve predicted by the simplified model is almost coincident with the curve predicted by the finite element simulation. However, after UTS the evolution of voids predicted by the finite element model accelerates while a smooth increase is observed in the simplified model curve. This is because of the fact that the simplified model does not consider the coalescence of voids. Thus, as mentioned before, the simplified model provides realistic results until reaching UTS and it cannot be used beyond UTS.

4- 2- Parameter study

The simplified model of the tensile test was used to evaluate the effect of GTN parameters on the evolution of voids and also on the tensile force. Six parameters were considered including f_0, q_1, q_2, f_N, S_N and $\bar{e}_N^{(p)}$. For each of these parameters, lower and upper limit values were selected based on literature [18, 19]. When assessing the effect of a particular GTN parameter on the void and force evolutions, the other parameters were kept fixed at the mean of their lower and upper limits. Table 3 shows the lower, mean, and upper values of the above-mentioned GTN parameters.

The effect of GTN parameters on the evolution of voids during the uniaxial tensile test is depicted in Fig. 4. As shown in Fig. 4(a), f_0 has no effect on the rate of voids evolution.

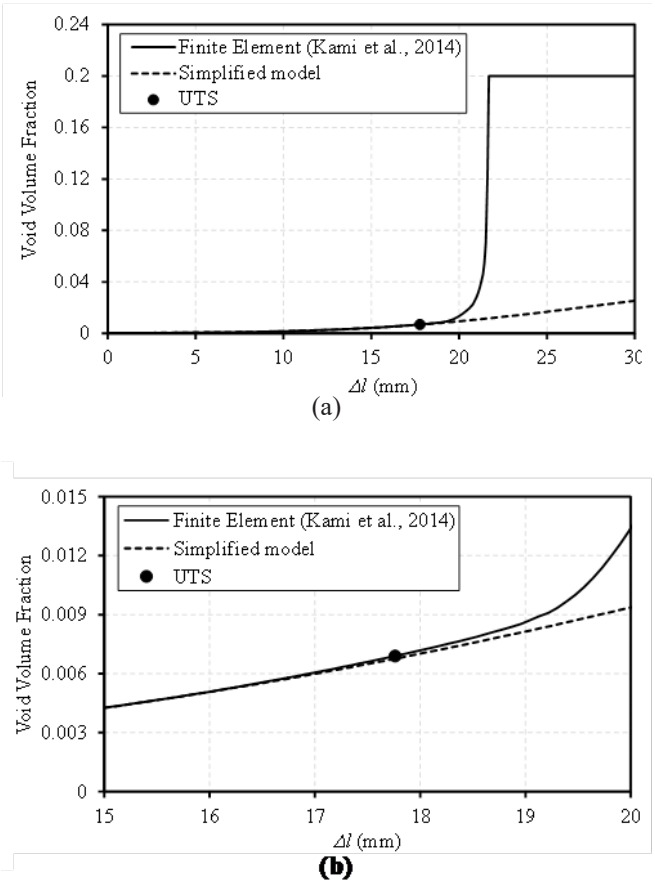

Fig. 3. Comparison of voids evolution calculated by the simplified model with results of the finite element model of Kami et al. [16].

But, it is obvious that the sample with higher f_0 will have higher values of f at each deformation stage and will probably fracture at lower strains. An increase in the value of q_1, q_2 and f_N accelerates the voids evolution (see Fig. 4 (b), (c) and (d)). Fig. 4 (e) shows that when the value of S_N is equal to 0.010, the slope of voids evolution curve is very small. Also, a sudden change occurs in its slope at about Δl=25 mm. So, one may conclude that higher values of S_N are more desirable because such higher values result in smooth void evolutions. Based on literature, the common value of S_N is 0.1. Furthermore, Fig. 4 (f) shows that increasing $\bar{e}_N^{(p)}$ from 0.05 to 0.50 changes both the curvature and slope of the voids evolution curve, the higher the value of $\bar{e}_N^{(p)}$ the lower the value of voids evolution curve. On the other hand, by increasing $\bar{e}_N^{(p)}$ the voids nucleation will be delayed.

The anisotropic GTN model allows to study the effect of

Table 3. The lower, mean, and upper values of GTN parameters.

Parameter	Lower limit	Mean	Upper limit
f_0	0.000	0.025	0.050
q_1	1.0	1.5	2.0
q_2	0.5	1.0	1.5
f_N	0.000	0.025	0.050
S_N	0.010	0.105	0.200
$\bar{e}_N^{(p)}$	0.050	0.275	0.500

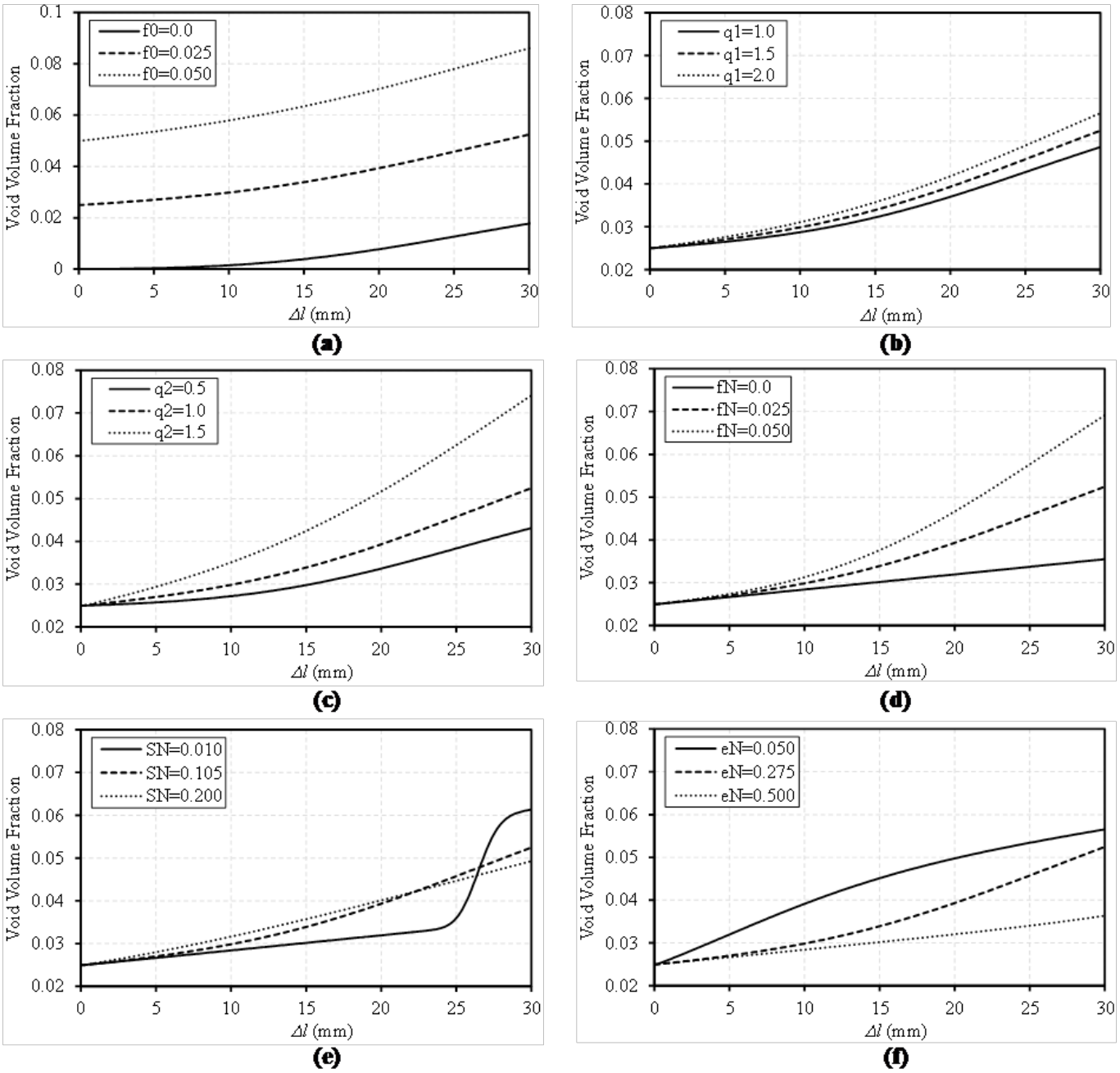

Fig. 4. Effect of, (a) initial void volume fraction, f_0, (b) adjusting parameter, q_1, (c) adjusting parameter, q_2, (d) nucleation void volume fraction, f_N, (e) standard deviation, S_N and (f) mean value of void nucleation strain, $e_N^{(p)} - \bar{e}_N$, on the evolution of voids during the uniaxial tensile test.

specimen orientation with respect to the rolling direction, θ, on the evolution of voids. The simplified tensile test model was used to assess the effect of θ on voids evolution in uniaxial tensile testing of AA6016-T4 sheet (see Fig. 5 (a)). As one may notice from Fig. 5 (a), the void evolution curves corresponding to θ=0° and θ=90° are almost coincident. This is because of the fact that the anisotropy coefficients r_0=0.5529 and r_{90}=0.5497 have very close values. On the other hand, because r_{45} is quite different from r_0 and r_{90} the void evolution curve corresponding to θ=45° is also different from the ones associated to θ=0° and θ=90°. Furthermore, Fig. 5 (a) implies that when the tensile test is conducted in a direction with a lower r-value, i.e., θ=45°, the evolution of voids is characterized by a higher speed. To investigate the latter observation, the Lankford coefficients of the sheet were set to r_0=0.5, r_{45}=1.0 and r_{90}=1.5, and tensile tests at θ=0°, θ=45° and θ=90° directions were simulated (see Fig. 5 (b)). Fig. 5 (b) confirms that the lower the r-value the higher the void evolution rate, i.e., because r_0=0.5 < r_{45}=1.0 < r_{90}=1.5 the void evolution rate corresponding to θ=0°>θ=45°>θ=90°. Besides the void evolution curves, force-displacement curves of the tensile test have been calculated using the simplified model. Fig. 6 depicts the effect of f_0, q_1, q_2, f_N, S_N and $\bar{e}_N^{(p)}$ on the force-displacement curve. As one may notice from Fig. 6, all the parameters, except S_N, have noticeable effects on the tensile force. Furthermore, Fig. 6 shows that increasing

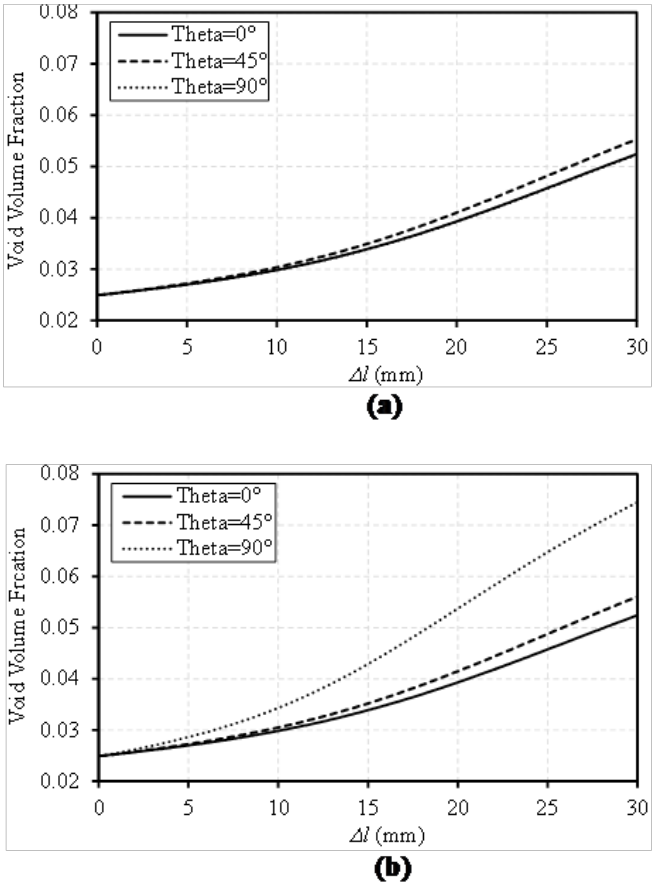

Fig. 4. Effect of specimen orientation with respect to the rolling direction on the evolution of voids during the uniaxial tensile test. (a) Lankford coefficients correspond to AA6016-T4 sheet and (b) Lankford coefficients are set to r_0=0.5, r_{45}=1.0 and r_{90}=1.5.

f_0, q_1, q_2, and f_N and decreasing $\bar{e}_N^{(p)}$ yield in the tensile force reduction. In order to get a quantitative information on the changes of the force-displacement curves, the UTF and UTD values have been extracted from the curves in Fig. 6 and listed in Table 4. In this table, lower limit, mean, and upper limit are referring to the lower limit, the mean, and the upper limit of the GTN model parameters (see Table 3). Consequently, the values mentioned in Table 4 are the UTD and UTF values calculated at the three levels of the GTN model (lower limit, mean, and upper limit). As one may notice, the UTD and UTF values under the mean column of Table 4 (19.898 mm and 5298.443 N, respectively) are the same. This is because of the fact that these UTD and UTF values are calculated for the mean value of all GTN parameters. In agreement with the conclusions drawn from Fig. 6, Table 4 shows that UTF decreases when f_0, q_1, q_2, f_N, and S_N increase and $\bar{e}_N^{(p)}$ decreases. Moreover, Table 4 indicates that increasing f_0, q_1, q_2, and f_N results in a reduction of UTD. On the other hand, the lowest value of UTD corresponds to the mean values of S_N and $\bar{e}_N^{(p)}$. Finally, the effect of θ on the traction force has been investigated. Fig. 7 (a) shows the force-displacement curves of AA6016-T4 sheet in the 0°, 45° and 90° directions. According to this figure, the simplified model is able to capture the effect of the specimen orientation with respect to the rolling direction on the traction force. Because r_0=0.5529 and r_{90}=0.5497 are close to each other, the traction forces corresponding to 0° and 90° directions are almost coincident (Fig. 7 (a)). To illustrate the deviation in force-displacement curve with the change of specimen orientation, the Lankford coefficients are set to r_0=0.5, r_{45}=1.0 and r_{90}=1.5 (see Fig. 7 (b)). According to Fig. 7 (b), the highest forming force corresponds to the direction with the highest *r*-value, i.e., 90° direction.

5- Conclusions

No doubt that the main advantage of the GTN models is their ability to predict the damage and fracture during loading. But the results obtained in this research showed that the material parameters included in GTN models have different effects in the early stages of deformation. The simplified model of the tensile test developed by the authors was able to predict the traction force and voids content with high accuracy and with an efficient computation time and cost. The simplified model predicted the experimental UTF of AA6016-T4 sheet (5604.24 N) with a small error of 0.58%. The model was also able to predict the experimental UTD (17.76 mm) with an error of 9.44%. The simplified model shows that an increase in the values of q_1, q_2, and f_N results in accelerating the voids evolution. Furthermore, the results show that by changing $\bar{e}_N^{(p)}$ from 0.05 to 0.50 the curvature and slope of the voids evolution curve also change. Moreover, UTF decreases when f_0, q_1, q_2, f_N, and S_N increase and $\bar{e}_N^{(p)}$ decreases. Also, it was found that increasing f_0, q_1, q_2, and f_N caused the reduction of UTD. The lowest level of UTD was achieved at the mean values of S_N and $\bar{e}_N^{(p)}$. The main advantage of the simplified model is its ability to capture the influence of the specimen orientation on the force and void evolution curves. This ability allows applying the model to orthotropic sheets. It is worth mentioning that, after calibrating f_0, q_1, q_2, f_N, S_N, and $\bar{e}_N^{(p)}$ parameters using the simplified model of the tensile test, one may find values of f_C and f_F parameters using a trial-and-error procedure.

Table 4. Change in UTD and UTF with the change of GTN parameters.

Parameter	UTD (mm)			UTF (N)		
	Lower limit	Mean	Upper limit	Lower limit	Mean	Upper limit
f_0	20.384	19.898	19.414	5586.202	5298.443	5017.645
q_1	21.486	19.898	18.453	5449.656	5298.443	5138.335
q_2	20.628	19.898	18.214	5354.204	5298.443	5175.710
f_N	23.226	19.898	17.976	5378.990	5298.443	5238.972
S_N	22.975	19.898	20.995	5378.776	5298.443	5292.798
$\bar{e}_N^{(p)}$	21.733	19.898	22.975	5206.064	5298.443	5377.181

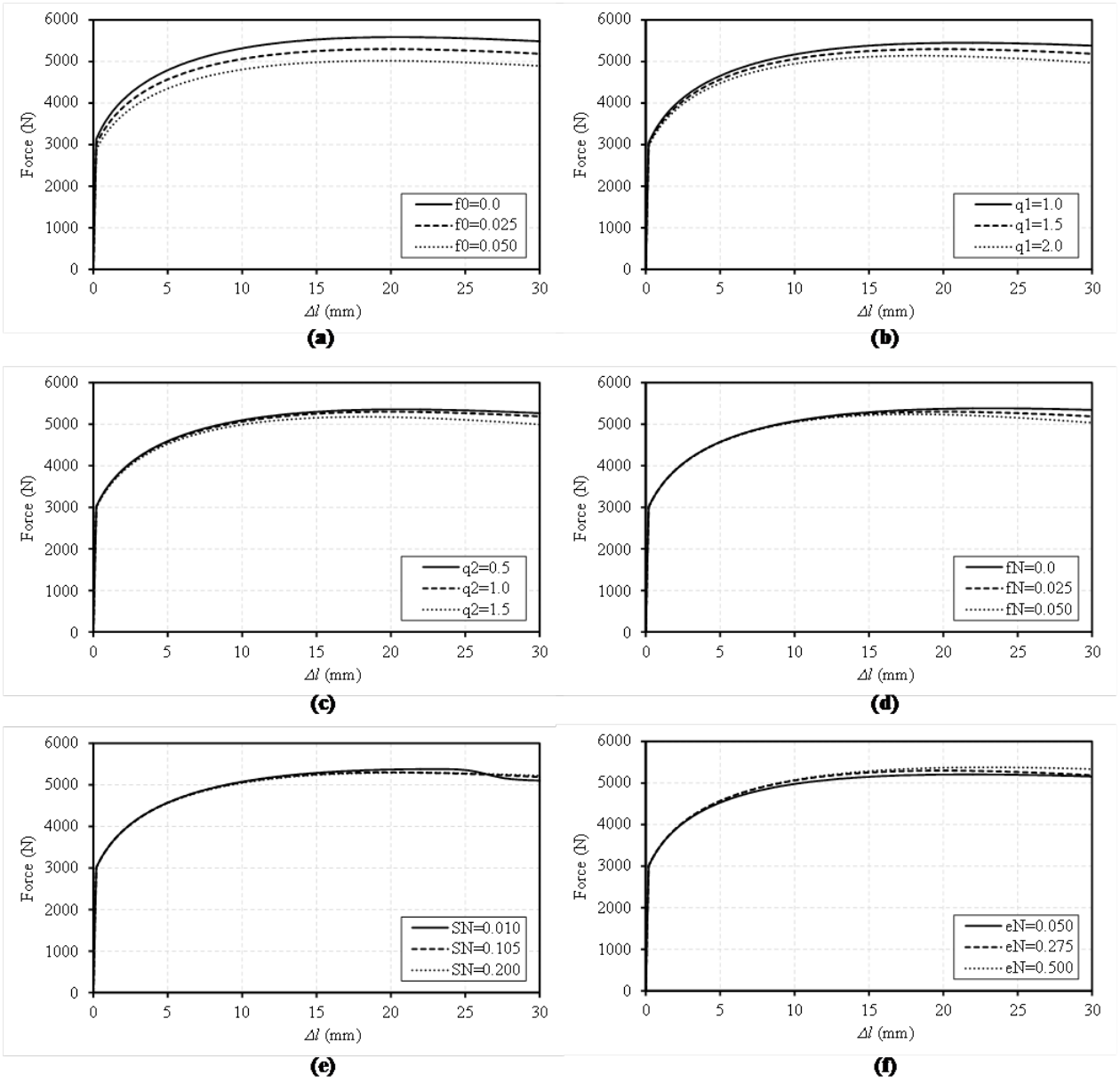

Fig. 6. Effect of (a) initial void volume fraction, f_0, (b) adjusting parameter, q_1, (c) adjusting parameter, q_2, (d) nucleation void volume fraction, f_N, (e) standard deviation, S_N, and (f) mean value of void nucleation strain, $\bar{e}_N^{(p)}$ - e_N on the uniaxial tensile test force.

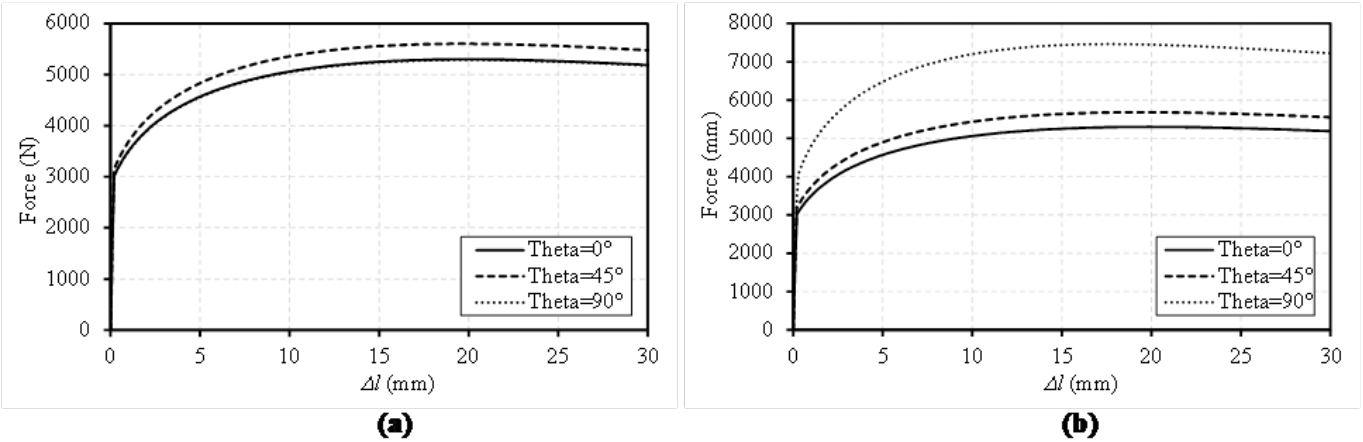

Fig. 7. Effect of specimen orientation with respect to the rolling direction on the traction force. (a) Lankford coefficients correspond to AA6016-T4 sheet and (b) Lankford coefficients are set to r_0=0.5, r_{45}=1.0 and r_{90}=1.5.

References

[1] C. Tipper, *The fracture of metals, Metallurgia*, 39(231) (1949) 133-137.

[2] K. Puttick, *Ductile fracture in metals, Philos. Mag.*, 4(44) (1959) 964-969.

[3] F.A. McClintock, A criterion for ductile fracture by the growth of holes, *Journal of Applied Mechanics*, 35(2) (1968) 363-371.

[4] J.R. Rice, D.M. Tracey, On the ductile enlargement of voids in triaxial stress fields, *J. Mech. Phys. Solids*, 17(3) (1969) 201-217.

[5] A.L. Gurson, Continuum theory of ductile rupture by void nucleation and growth Part I-Yield criteria and flow rules for porous ductile media, *J. Eng. Mater. Technol.*, 99(1) (1977) 2-15.

[6] V. Tvergaard, Influence of voids on shear band instabilities under plane strain conditions, *Int J Fracture*, 17(4) (1981) 389-407.

[7] V. Tvergaard, A. Needleman, Analysis of the cup-cone fracture in a round tensile bar, *Acta Metall.*, 32(1) (1984) 157-169.

[8] K. Nahshon, J.W. Hutchinson, Modification of the Gurson model for shear failure, *European Journal of Mechanics - A/Solids*, 27(1) (2008) 1-17.

[9] A. Kami, B.M. Dariani, A. Sadough Vanini, D.S. Comsa, D. Banabic, Numerical determination of the forming limit curves of anisotropic sheet metals using GTN damage model, *J. Mater. Process. Technol.*, 216(0) (2015) 472-483.

[10] Z. Chen, X. Dong, The GTN damage model based on Hill'48 anisotropic yield criterion and its application in sheet metal forming, *Comp Mater Sci*, 44(3) (2009) 1013-1021.

[11] M. Abendroth, M. Kuna, Identification of ductile damage and fracture parameters from the small punch test using neural networks, *Eng Fract Mech*, 73(6) (2006) 710-725.

[12] G. Broggiato, F. Campana, L. Cortese, Identification of material damage model parameters: an inverse approach using digital image processing, *Meccanica*, 42(1) (2007) 9-17.

[13] A. Kami, B. Mollaei Dariani, D.-S. Comsa, D. Banabic, A. Sadough Vanini, M. Liewald, Calibration of GTN damage model parameters using hydraulic bulge test, *Rom. J. Techn. Sci. Appl. Mechanics*, 61(3) (2016) 248-264

[14] H.H. Nguyen, T.N. Nguyen, H.C. Vu, Ductile fracture prediction and forming assessment of AA6061-T6 aluminum alloy sheets, *Int J Fracture*, 209(1) (2018) 143-162.

[15] M. Abbasi, M.A. Shafaat, M. Ketabchi, D.F. Haghshenas, M. Abbasi, Application of the GTN model to predict the forming limit diagram of IF-Steel, *J Mech Sci Technol*, 26(2) (2012) 345-352.

[16] A. Kami, B. Mollaei Dariani, A. Sadough Vanini, D.-S. Comsa, D. Banabic, Application of a GTN Damage Model to Predict the Fracture of Metallic Sheets Subjected to Deep-Drawing, *Proc Rom Acad Ser A*, 15(3) (2014) 300-309.

[17] R. Hill, A theory of the yielding and plastic flow of anisotropic metals, *Proc R Soc Lond A-Math Phys Eng Sci*, 193(1033) (1948) 281-297.

[18] R. Kiran, K. Khandelwal, Gurson model parameters for ductile fracture simulation in ASTM A992 steels, *Fatigue Fract Eng M*, 37(2) (2013) 1-13.

[19] N. Benseddiq, A. Imad, A ductile fracture analysis using a local damage model, *Int J Pres Ves Pip*, 85(4) (2008) 219-227.

Please cite this article using:

A. Kami and D.-S. Comsa, A Simplified Description of the Uniaxial Tensile Test Used for Calibrating Constitutive Models of Orthotropic Porous Sheet Metals, *AUT J. Mech. Eng.*, 2(2) (2018) 127-136.

DOI: 10.22060/ajme.2018.13862.5693